

Accepted Article

Title: Investigation on the structure and performance of supported Ni nanoparticles for the hydrogenation of furfural

Authors: Xiaowei Chen, Shahram Alijani, Simone Gallarati, Francesca Tessore, Juan Jose Delgado Jaen, Diego Gianolio, Alberto Villa, and Rosa Arrigo

This manuscript has been accepted after peer review and appears as an Accepted Article online prior to editing, proofing, and formal publication of the final Version of Record (VoR). The VoR will be published online in Early View as soon as possible and may be different to this Accepted Article as a result of editing. Readers should obtain the VoR from the journal website shown below when it is published to ensure accuracy of information. The authors are responsible for the content of this Accepted Article.

To be cited as: *ChemCatChem* **2024**, e202400229

Link to VoR: <https://doi.org/10.1002/cctc.202400229>

RESEARCH ARTICLE

Investigation on the structure and performance of supported Ni nanoparticles for the hydrogenation of furfural

Xiaowei Chen,^[b] Shahram Alijani,^[c] Simone Gallarati,^[d] Francesca Tessore,^[c] Juan Jose Delgado,^[b] Diego Gianolio,^[d] Alberto Villa,^{*[c]} Rosa Arrigo^{*[a,d]}

[a] Dr. R., Arrigo

School of Science, Engineering and Environment, University of Salford,
Peel Building 336, M5 4WT, Manchester
E-mail: r.arrigo@salford.ac.uk

[b] Dr X. Chen and Dr. J.J. Delgado

Departamento de Ciencia de los Materiales, Ingeniería Metalúrgica y Química Inorgánica, Facultad de Ciencias, Universidad de Cádiz, Campus Río San Pedro, Puerto Real, Cádiz E-11510, Spain

[c] Dr. S. Alijani, Dr. F. Tessore and Dr. Alberto Villa

Dipartimento di Chimica, Università degli Studi di Milano
Via Golgi 19, 20133 Milano, Italy
E-mail: alberto.villa@unime.it

[d] Dr. R., Arrigo, Dr. D. Gianolio and Dr. S. Gallarati,

Diamond Light Source,
Harwell Science and Innovation Campus, OX11 0DE, Oxfordshire, UK

Supporting information for this article is given via a link at the end of the document.

Abstract: In this study, nickel (Ni) nanoparticles were successfully synthesised using two methods: the hot-injection method and a room temperature colloidal synthesis using dioctyl tartrate as a capping agent. Each approach yielded Ni nanoparticles with unique morphological and electronic properties. The distinct characteristics of these Ni nanoparticles make them promising candidates for unravelling structure/activity relationships, a crucial aspect in developing catalysts with enhanced selectivity. Furthermore, Ni nanoparticles synthesized via these methods were supported on both silica and activated charcoal, with variations in Ni loadings. We explored the impact of nanostructural characteristic of the Ni NPs as well as support effects on the selective hydrogenation of furfural. Using temperature programmed reduction, advanced X-ray absorption spectroscopy, and atom-resolved electron microscopy techniques, we established comprehensive structure-function relationships. Herein, we demonstrate that using a dioctyl tartrate route, foam-like Ni nanostructures are obtained, yielding higher selectivity towards selective hydrogenation than commercial Ni/Al₂O₃ and a suppression of the acid-catalysed acetalization and etherification reactions. Furthermore, conversions similar to commercial Ni/Al₂O₃ are achieved using a lower Ni loading. These insights provide valuable guidance for the design of enhanced materials, contributing to the optimization of catalyst performance in selective hydrogenation processes. This research marks a significant step toward the development of more efficient and sustainable catalytic processes.

Introduction

The conversion of biomass into platform chemicals represents a promising pathway for the sustainable synthesis of fine chemicals

and fuels.^[1,2] An essential aspect of biomass utilisation is the harnessing of readily available sources that are not integral to the food chain.^[3] Lignocellulosic biomass, comprising cellulose (40–50%), hemicellulose (20–35%), and lignin (15–25%), stands out as one of the most sustainable sources owing to its abundant availability and non-edible nature.^[4]

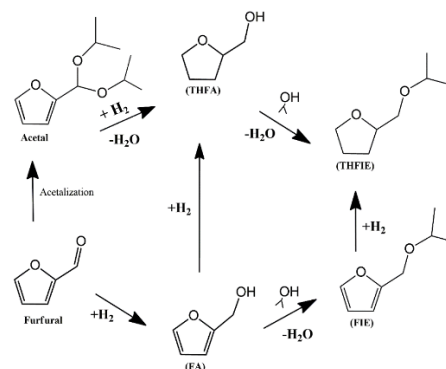


Figure 1. Schematic representation of the possible reaction pathways of the furfural hydrogenation: furfuryl alcohol (FA), tetrahydrofurfuryl alcohol (THFA), furfuryl isopropyl ether (FIE), and tetrahydrofurfuryl isopropyl ether (THFIE).

Furfural, obtained via acid-catalysed cascade hydrolysis and dehydration of lignocellulose^[5], emerged as a versatile platform chemical with considerable potential for producing a diverse array of valuable chemicals. Its abundance, cost-effectiveness, and the high reactivity of structural functional groups, such as the aldehyde group and the furan ring with α,β -unsaturation^[6–8],

RESEARCH ARTICLE

position furfural as an ideal feedstock for subsequent chemical processing. Depending on the nature of the active metal in the catalyst and its nanostructural characteristics, including distribution of exposed active sites such as edges, corners, terraces, the furfural molecules can be adsorbed onto the metal surface through their functional groups, carbonyl group and furan ring, forming a variety of products (Figure 1).^[9] Furfuryl alcohol (FA) can be obtained via hydrogenation of the furfural carbonyl group, and it is widely used for producing resins, lubricants, plasticizers and fibers.^[10] The hydrogenation of both carbonyl group and furan ring produces tetrahydrofurfuryl alcohol (THFA), a green solvent used in printer inks and agriculture applications.^[11] When subjected to hydrogenation conditions on metal catalysts, the aromatic furan ring tends to adhere firmly to the metallic surface. In these cases, furfural hydrogenation results in the dominant production of furan and tetrahydrofuran (THF) through decarbonylation and ring hydrogenation.^[12-14] Ethers can also be formed in the presence of acid sites, resulting in the production of compounds used as fuel-additives or surfactants. Furfural derived ethers can be obtained following two pathways: the first one is the direct etherification involving the saturation of C=O bond to C–OH and subsequently the acid-catalyzed intermolecular dehydration;^[15] the second one is the reductive-etherification involving the acetalization of aldehydes as an intermediate acetal compound and the subsequent hydrogenolysis and/or dehydration-hydrogenation of the acetal to form the final ether, as shown in Figure 1.^[16]

A variety of noble metal-based catalysts were reported effective for the hydrogenation of furfural,^[17] including Pt,^[18] Pd,^[19] Rh,^[20] Ir,^[21] and Ru.^[22] Supported catalysts based on transition metals, such as Ni, Cu, Cr, and Co, are preferable because of their abundance and low cost.^[13] Supported metal nanoparticles (NPs) offer many opportunities to tailor the selectivity of the process through specific metal/support interaction.^[23,24] Nickel-based catalysts are considered as an excellent system for furfural conversion, owing to the ability of Ni to activate both the carbonyl group and the furan ring.^[25] Ni-based catalysts offer some advantages such as a lower environmental impact compared to Cr and lower operational H₂ pressures.^[1] Nevertheless, a significant drawback of these catalysts is their low selectivity and poor stability.^[25] Therefore, the main challenge in furfural hydrogenation lies in effectively controlling its reaction pathway to maximize selectivity. Kotbagi *et al.* reported 96% of furfural conversion and 95% FA selectivity at 200 °C and 10 bar H₂ using Ni supported on N-doped hierarchically porous carbon catalyst.^[14] Jeong *et al.* observed a similar selectivity to FA and THFA for Ni/SiO₂ and Raney Ni at 110 °C and 30 bar H₂.^[26] Ni-metal-organic framework (Ni-MOF) derived catalysts afforded a 92.5% conversion of furfural and a 59.5% selectivity to FA at 160 °C and 20 bar H₂.^[13] A series of 10 wt.% Ni/CNT catalysts prepared by wet impregnation showed high conversion of furfural (99.1 %) and selectivity towards THFA (85.1 %).^[27] Full conversion and total selectivity (99.9 %) to FA were achieved using sulfonate group-modified activated carbon supported Ni catalyst (Ni/AC-SO₃H) prepared via the liquid phase reduction method.^[28] Yet, these processes require high hydrogen pressure that adds further complexity and operation cost to the process.

Compared to conventional synthetic routes such as wet impregnation, sol-immobilization affords mono-dispersion and smaller average particle size.^[24] Carencio *et al.* used alkylamine and phosphine-containing capping ligand to produce monodisperse Ni NPs with a tunable particle size varying from 2 to 30 nm.^[29]

Colloidal particles offers opportunity for selective catalysis owing to the use of size-controlling and shape-inducing ligands, which at the same time enable a tuning of the exposed surface area. For instance, Rinaldi *et al.* prepared colloidal Ni NPs supported on silica with enhanced performances in hydrogenation of cyclohexene and ethanol steam reforming.^[30] Silica-Supported Ni nanoparticles below 4 nm in diameter gave higher turnover frequency for furfural hydrogenation than other supported Ni catalysts.^[31] Meng *et al.* found that high exposure of Ni(111) planes in Ni/MMO-CO₃ enables adsorption of both the furan ring and C=O group and favors the production of a fully hydrogenated product.^[32] Controlling particle size, shape, and dispersion through colloidal synthesis has the potential to reduce the operating pressure for the hydrogenation reaction and enhance selectivity.^[24, 33] Notwithstanding these advantages, studies on the use of the colloidal approach for the preparation of supported Ni NPs catalysts for furfural hydrogenation are limited.

A critical aspect to consider is also the conversion, which for colloidal NPs might be lower than conventional catalysts obtained via ligand-free routes.

In the present work, we investigate the reactivity in furfural hydrogenation of Ni based systems obtained via two different synthetic routes: i) hot-injection route which uses oleylamine as mild reducing agent and a bulky, branched, trioctyl phosphine as a capping agent; ii) colloidal synthesis at milder temperature using a stronger reducing agent, namely sodium borohydride, and a linear long-chain ligand, as a capping agent, namely dioctyl tartrate. The first method is well-established for the synthesis of unsupported metal nanoparticles at mild condition.^[34] Our choice of the dioctyl tartrate as a capping agent derived from the consideration that tartaric acid used as a ligand promotes a better dispersion and inhibits the aggregation of Ni NPs.^[35] Furthermore, owing to its affinity towards coordinating Ni(II) species, tartaric acid could also act as a leachant.^[36] We reckon that this property could induce the exposure of specific metal sites. We therefore developed a synthesis which uses dioctyl tartrate: the long-chain hydrophobic part of the ligand enables controlling the particles size and shape during the synthesis; the tartrate termination enables a tuning over the exposed surface area during reaction via a partial detachment from the surface through its chelating effect to Ni atoms. These two methods afforded Ni nanostructures exhibiting distinct morphological and electronic characteristics, and therefore are ideal systems for elucidating structure/activity relationships, crucial for the development of more selective and stable catalysts. By employing advanced X-ray spectroscopy and atom-resolved electron microscopy techniques, we explore various aspects ultimately influencing performances such as metal-support interactions, metal loading and other catalysts pre-treatments. Whilst this work will not capture the nature of the catalyst active sites under operation conditions requiring *in situ* approaches, it will highlight the temporal evolution of the catalytic

RESEARCH ARTICLE

behavior of materials with specific nanostructural characteristics in a precursor state of the catalysts. We thus establish precursor structure-catalytic function relationships to guide the design of enhanced materials.

Results and Discussion

A series of unsupported and supported Ni NPs-based catalysts were synthesised via the hot-injection method using oleylamine (OAm) as the reducing agent and trioctylphosphine, (TOP) as the protecting agent, as described in the experimental section.

Table 1. Summary of synthesis conditions of Ni catalysts.

Sample	Ni/ wt. % ^[i]	Ni/ wt. % ^[ii]	Ni(acac) ₂ / g	ODE / mL	OAm / mL	TOP / mL
Ni- <i>hi</i>			0.8764	17.5	5.6	2.3
Ni _{5%} /AC ^[a]	5	-	0.8764	17.5	5.6	2.3
Ni _{5%} /AC ^[b]	5	-	0.8766	6.5	16.8	2.3
Ni _{5%} /AC/ Ni _{5%} /AC ^[d]	5	3±0.02 2.3±0.1	0.8760	17.5	5.6	2.3
Ni _{5%} /SiO ₂	5	3.1±0.1	0.8764	17.5	5.6	2.3
Ni _{10%} /SiO ₂	10	-	1.7528	34.9	11.2	4.6
Ni _{20%} /SiO ₂	20	-	3.5	70	22.4	9.2
Ni _{10%} /SiO ₂ ^[e]	10	-	1.7522	35	11.2	2.3
Ni _{10%} /SiO ₂ ^[f]	10	-	1.755	35	11.2	9.2
			NiBr ₂ / g	DT / g	NaBH ₄ / g	
Ni- <i>dt</i>			0.5980	0.772 1	0.5190	
Ni/SiO ₂ - <i>dt</i>	20	16.0±0. 2	0.5980	0.772 1	0.5190	
Ni/SiO ₂ - <i>dt</i> - sm ^[c]	20	16.0±0. 4	0.5980 ^[g] +2.8321 ^[h]	0.772 1 ^[g] +3.6 265 ^[h]	0.5190 [g] +2.440 9 ^[h]	

[a] The NPs synthesis was performed for 3h sample; after the NPs immobilization, the sample was heated to 370°C under N₂, then reduced in H₂ for 2h. [b] The NPs synthesis was performed for 1h. [c] Seed mediated synthesis. The total nominal loading is 20 % in weight, but the NPs synthesized according to the 10% loading were used to growth NPs on them using a mixture composition leading to an additional 10% in weight. [d] 3h synthesis. [e] 0.75 eq. TOP [f] 3 eq. TOP. [g] Seed solution and [h] growth solution. [i] Nominal loading in weight percentage. [j] Ni loading determined by ICP-OES technique.

In the dioctyl tartrate (DT) route, sodium borohydride was used as the reducing agent. Sketches of these syntheses are shown in scheme 1 and 2, respectively. A complete list of the samples prepared is presented in Table 1. The Ni loadings of some supported catalysts are lower than nominal values. This discrepancy may be attributed to organic residue present on the samples, which is not accounted for in the calculation of the nominal loading.

Reactivity data

Figure 2 reports the furfural conversion and the selectivity at 25% conversion for the catalysts investigated in this work. The activity at 15 minutes of reaction is reported in Table S1. The evolution of the conversion with time unveils a striking difference in performances between the unsupported NPs prepared via hot-injection and via dioctyl-route, which is mostly retained after immobilization of the colloidal NPs on different supports.

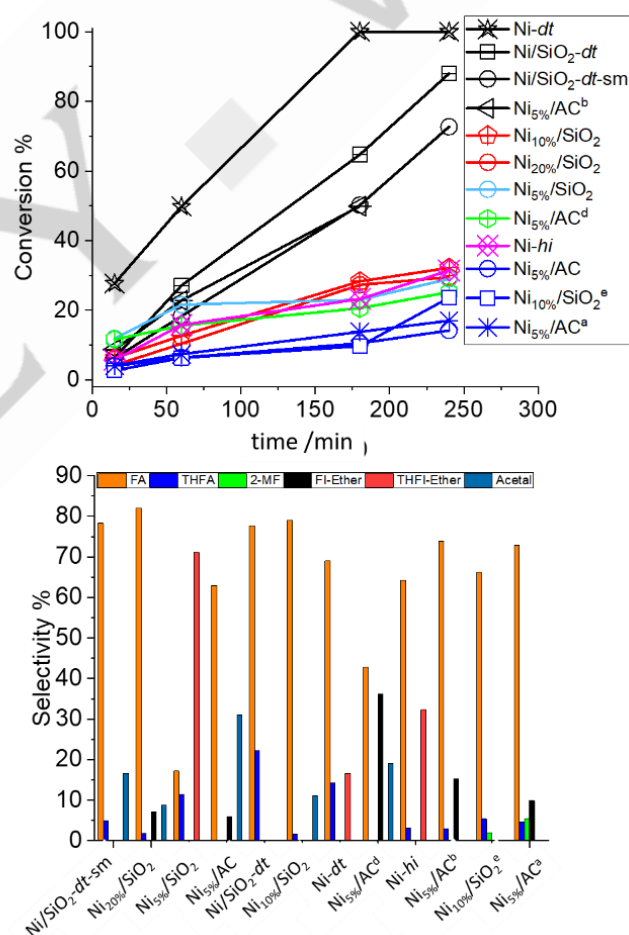


Figure 2. Furfural conversion vs time of reaction at 6 bar H₂ and 180 °C for the samples investigated as indicated (top); Selectivity at 25% furfural conversion (bottom).

RESEARCH ARTICLE

The unsupported nanoparticles prepared using dioctyl tartrate as a capping agent showed the highest activity (480 h^{-1}) compared to the Ni NPs prepared by hot injection (100 h^{-1}), (Table S1 and Figure S1). The best performing supported catalysts, in terms of activity, are Ni_{5%}/SiO₂ and Ni_{5%}/AC^d with a very similar activity of 199 h^{-1} and 209 h^{-1} , respectively. A NPs synthesis carried out for longer time (3h) in Ni_{5%}/AC^d led to a slightly higher conversion, achieved after 60 minutes of reaction, which remains unchanged for the entire period of time investigated, suggesting that the catalyst is nevertheless prone to deactivation. Ni_{5%}/AC^a, which derives from Ni_{5%}/AC^d but was additionally subjected to a reduction step prior furfural hydrogenation, is characterized by an extremely low conversion remaining almost unchanged for the entire time reaction. Similar behavior was observed for Ni_{5%}/SiO₂ with a total conversion reaching a value of approximately 22% after 60 minutes of reaction, followed by a deactivation/reactivation that yield a maximum conversion of 29% after 240 minutes of reaction. A pronounced deactivation of Ni/TiO₂-SiO₂ catalysts at reaction temperature higher than 100 °C and pressure of 10 bar was found due to C-C cracking and coking.^[37] In contrast, Ni_{10%}/SiO₂ and Ni_{20%}/SiO₂ present a slow but steady increase of the conversion, which reaches the maximum value of approximately 30% after 240 minutes of reaction. These samples were synthesised using same reducing/capping agent ratio (5 equivalents of OAm and 1.5 equivalents of TOP) in the NPs synthesis step as for Ni_{5%}/SiO₂, but using a proportionally higher amount of reagents, thus a similar average particle size and morphology is expected. The best results amongst the hot-injection samples in terms of conversion and selectivity were obtained for Ni_{5%}/AC^b synthesised in a comparatively shorter reaction time than Ni_{5%}/AC, using a comparatively higher amount of the reducing agent OAm (15 eq. of OAm and 1.5 eq TOP) and thus a lower amount of the solvent, 1-octadecene. Ni nanoparticles obtained via hot injection are generally characterized by a low conversion under the mild reaction conditions used in this work, consistent with literature.^[38]

The effect of the H₂ pressure was studied by Kotbagi *et al.*^[14] on Ni/C systems obtained by co-gelation sol-gel technique. It was found that at 200 °C, furfural conversion was low at 2 bar H₂ pressure, reaching 30 % only after 6 hours of reaction, whereas it was enhanced at higher H₂ pressure, reaching a maximum of 100% at 10 bar. Total conversion of furfural was obtained over Ni/C systems at 3 bar and 140 °C.^[39] Comparing these results with those obtained for a commercial Ni_{18%}/Al₂O₃ catalysts under the same mild conditions (Table S1), it seems evident that more work is needed to fully exploit the hot-injection route for the generation of catalytic materials for this reaction and other green processes based on renewable feedstocks.

The dioctyl-route gives SiO₂-supported Ni catalysts performing better in terms of conversion, more so for Ni/SiO₂-*dt*, where the total conversion is achieved after 2 h of reaction at 6 bar and 180 °C, whereas the selectivity to FA reaches 80%. Note that in the synthesis of Ni/SiO₂-*dt*, 5 eq. of NaBH₄ and 0.75 eq. of DT are used, the latter one being a comparatively low amount. The performance of Ni/SiO₂-*dt* is very similar to that of Ni_{5%}/AC^b, demonstrating the important role of tailoring the amount of reducing agent/capping agent for enhancing performances. Also,

Ni-*dt* performs very similar to the commercial Ni_{18%}/Al₂O₃ system in terms of conversion kinetics (Table S1). A very important aspect to note in this study is that the selectivity distribution differs sufficiently amongst the samples investigated, therefore providing an excellent dataset to understand the reaction mechanism that informs materials and synthesis design.

In term of selectivity calculated at 25% conversion (Figure 2b), the main reaction product is FA for all the catalysts but Ni_{5%}/SiO₂, which produce predominantly tetrahydrofurfuryl isopropyl ether (THFI-E). FA is the product of the hydrogenation of the C=O group present in the furfural, whereas THFI-E derives from the unselective hydrogenation of both the carbonyl and the furan ring followed by the condensation reaction with isopropyl alcohol to form the ether. This finding indicates that specific functionalities of the catalysts can dictate the course of the reaction; these need to be understood for improved catalyst design.

It is useful to have a closer look at the time dependence of the selectivity reported in Figure S1 and Table S1 for all the samples investigated.

For the dioctyl route, the highly active, unsupported sample is selective for the hydrogenation of furfural from the beginning of the reaction and remains so for the entire time of reaction, although the subsequent hydrogenation to THFA and solvent condensation to THFI-E become more favored with time. On Ni/SiO₂-*dt* and Ni/SiO₂-*dt*-sm, the consecutive formations of the THFA and the THFI-E are suppressed, and at the same time a decrease of activity and conversion is observed. The latter two samples differ in terms of loading (10% and 20%, respectively) but the performances did not change proportionally, similarly to the Ni_{10%}/SiO₂ and Ni_{20%}/SiO₂, indicating that not all the particles surface area is accessible. On Ni/SiO₂-*dt*, the almost exclusive selectivity towards hydrogenation, makes it a very promising system outperforming the less selective commercial material tested here.

The unsupported NPs obtained via hot-injection route is equally selective towards the carbonyl hydrogenation of furfural to FA as well as the furan ring hydrogenation which subsequently undergoes condensation with isopropanol and formation of THFI-E in similar amount to FA. Due to the absence of acetal, we suggest that the THFA is formed via a subsequent reaction following FA formation, whereas the only etherification of THFA to THFI-E implies that the former remains adsorbed on the catalyst surface more strongly than FA.

However, with time the catalysts become more selective towards FA formation; as earlier suggested, this could be a consequence of the deactivation of the catalyst. In the case of Ni_{5%}/AC and Ni_{5%}/AC^d, similar products are obtained with a different distribution, although Ni_{5%}/AC^d is much more active than Ni_{5%}/AC (the activity is 66 h^{-1}). For these catalysts, the acetalization reaction occurs first, whereas FA become the most favored reaction pathway only at longer reaction time. Ni_{5%}/AC^d produces also FIE with a selectivity that increases with time indicating that the condensation of the solvent is parallel and successive to the hydrogenation reaction (Scheme 1). Thus, it can be inferred that initially the metal particles are protected by the C overlayer preventing hydrogen adsorption; however at longer reaction times, the detachment of the C overlayer from the particle surface and

RESEARCH ARTICLE

its dissolution in the reaction medium enables a higher exposed metal surface which facilitates the hydrogenation pathways. However, a poor hydrogenation capability can be also related to the reduction ability of the Ni phase. This is consistent with the results obtained for Ni_{5%}/AC^b synthesised using large amount of OAm, for which, the acetal is observed as a minor product only at very low conversion. Thus, we suggest that the acid-base catalysed acetal formation is a consequence of the poor Ni metallic character as well as the chemical characteristics of support and C-overlayer, in terms of acid-base properties. When the hot injection Ni NPs are immobilized on silica at 5% loading (5 eq. OAm and 1.5 eq. of TOP), the initial activity is high but the final conversion is low. The sample is rather an unselective hydrogenation catalyst, with the main product at the beginning of the reaction being THFI-E. Differently to the other hot injection samples, no acetal formation is observed here, thus we suggest that THFI-E is obtained via the FA pathway. The catalyst becomes more selective towards carbonyl hydrogenation with time as demonstrated by the slight decrease of productivity to FA, which is probably a consequence of its deactivation. Increasing the loading on silica in Ni_{10%}/SiO₂ and Ni_{20%}/SiO₂ (whilst maintaining the same equivalent ratio of reducing and capping agent) leads to a decrease of the activity and a change in selectivity distribution, resembling the hot-injection NPs on AC support, although FA selectivity is much higher than for AC-based catalysts, reaching approximately 80% at the end of the reaction. The impact of the equivalents of OAm and TOP can be discerned by comparing Ni_{10%}/SiO₂, Ni_{10%}/SiO₂^e and Ni_{10%}/SiO₂^f, which are synthesised using the same equivalents of OAm (5 equivalents) but different equivalents of TOP amounting to 1.5, 0.75 and 3, respectively. Despite the TOP amount is lower in Ni_{10%}/SiO₂^e, the performances are worsened in terms of conversion and selectivity to FA, indicating that not only the residual C overlayer influence the selectivity but other factors are at play mostly related to the Ni electronic structure influenced by the degree of reduction achieved by the reducing agent used as well as the interaction with the support.

Structural characterization of the catalysts

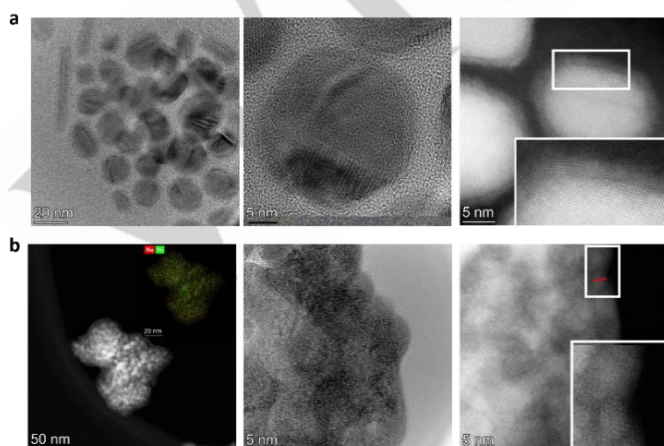


Figure 3. TEM and HAADF-STEM images of Ni-*hi* NPs synthesized by (a) hot-injection route and Ni-*dt* (b) diocetyl-route. Inset in b) depicts the Na and Ni elemental mapping determined by EDX analysis. Lines within in the circle indicate the approximate length of the columns of atoms within the particles.

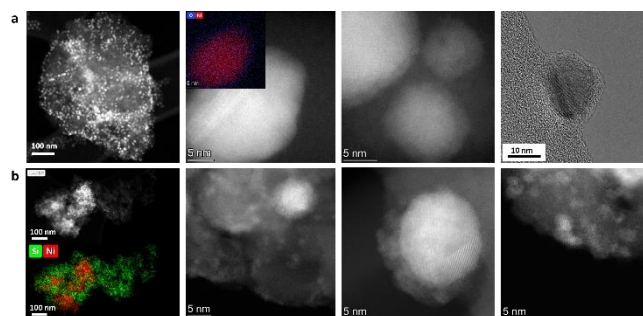


Figure 4. Ni NPs synthesized via hot-injection method supported on (a) Ni_{5%}/AC^d and (b) Ni_{5%}/SiO₂.

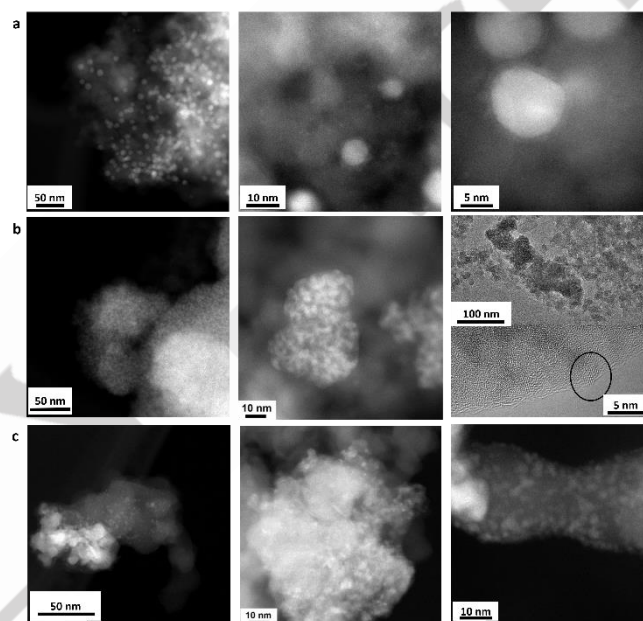


Figure 5. a) STEM-HAADF images of Ni_{20%}/SiO₂; b) STEM-HAADF image and HRTEM images (right) of Ni/SiO₂-*dt*; c) STEM-HAADF images of Ni/SiO₂-*dt-sm*.

The unsupported Ni NPs (Ni-*hi*) obtained by hot-injection (Figure 3a) present mainly primary twinned particles (clearly seen in the middle HRTEM image) of round morphologies covered with an overlay of secondary NPs with a much smaller diameter of approximately 1-2 nm (lower contrast shell in the right HAADF-STEM image). The diocetyl-tartrate route (Figure 3b) yields much smaller NPs of approximately 2-3 nm, agglomerated all together to form a porous microstructure. These results are consistent with the general observation in literature that stronger reducing agents such as sodium borohydride used in the second route leads to smaller particles [40] than weak reducing agents such as ethylamine.^[34] The EDX elemental mapping for this sample shows a homogeneous distribution of Na which derives from the NaBH₄ reducing agent (inset in Figure 3b).

The NPs obtained via hot-injection preserve their nanostructure when immobilized on activated carbon (Ni_{5%}/AC^d), as shown in the high angle annular dark field scanning transmission electron micrographs (HAADF-STEM) in Figure 4a, composed of the primary NP with an outer shell of secondary smaller NPs. A C-overlayer is clearly visible in the high resolution transmission

RESEARCH ARTICLE

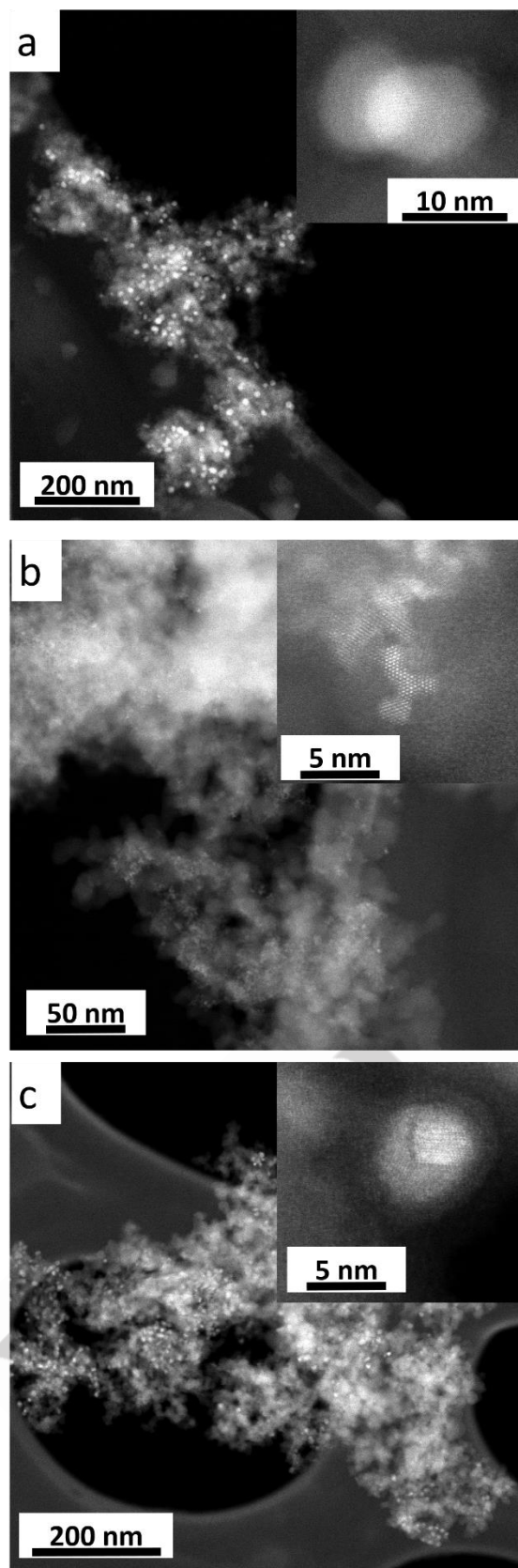


Figure 6. HAADF-STEM images for a) Ni₁₀%/SiO₂, b) Ni₁₀%/SiO₂^e and c) Ni₁₀%/SiO₂^f.

electron image in Figure 4a, which could explain the low conversion observed. A summary of the particle size distribution for the catalysts prepared via hot-injection is reported in Figure S2. We note that the average particle size is smaller for the supported samples indicating an interaction with the support that disrupt the primary colloidal solution during the immobilization step. Similar behavior was observed for colloidal Pd NPs immobilized on carbon nanotubes.^[40] In contrast, on Ni₅%/SiO₂, a bimodal distribution of NPs sizes is observed, consistent with the mobilisation of the small NPs from the overlayer region on the primary nanoparticles and dispersion onto the support; we suggest that this is due to stronger metal support interaction (SMSI) on this support compared to the C support.

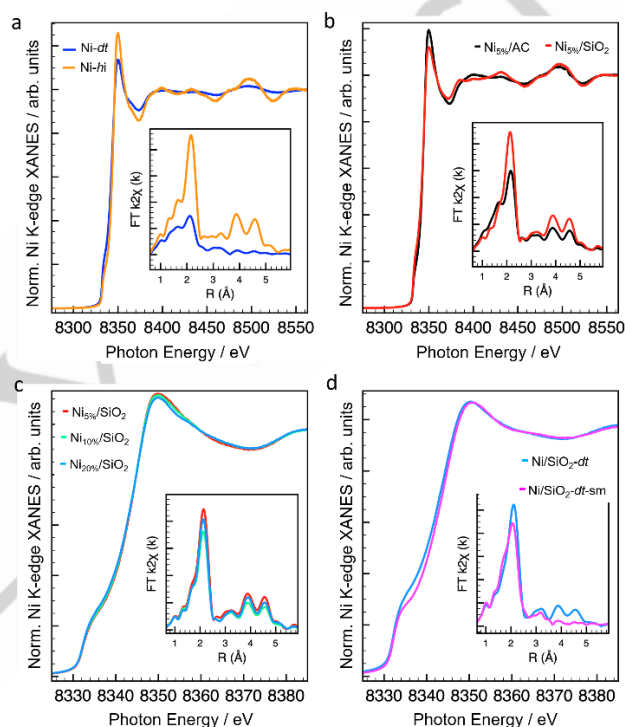


Figure 7. Ni K-edge XAFS analysis of: a) comparison of unsupported NPs; b) comparison of different supports; c) comparison of different loading; d) diocetyl tartrate synthesis route and subsequent seed-mediated synthesis.

Ni₂₀%/SiO₂ present a higher loading of NPs with a similar average particle size, but a more symmetric size distribution. No large differences can be identified with varying Ni loading, although the smaller highly dispersed NPs seen in Ni₅%/SiO₂ are less abundant for higher loaded samples. Ni/SiO₂-dt is characterized by the same agglomerated small Ni nanoparticles observed in the unsupported sample, packing into a hierarchical foam-like porous superstructure. Dense agglomerates of Ni particles can be clearly seen in the high resolution transmission electron microscopy (HRTEM) image in Figure 5b as a darker contrast than the SiO₂ support, which appears highly porous. The particles do not disperse on the support and therefore no electronic effects exerted by it are expected (Figure 5b top image on the right). The nanoparticle in the dense agglomerates are below 5 nm in size and embedded in a carbonaceous matrix (Figure 5b bottom image

RESEARCH ARTICLE

on the right), but also exposed and thus accessible to reagents as exemplified by the lattice fringes of the particles in the circle. The seed mediated synthesis on this sample (Ni/SiO₂-dt-sm in Figure 5c) leads to a more extreme size heterogeneity of the particle agglomerates. The impact of the TOP equivalents on the structural and morphological characteristic of the NPs has also been investigated by electron microscopy for the in the series Ni_{10%}/SiO₂, Ni_{10%}/SiO₂^e and Ni_{10%}/SiO₂^f and here reported in Figure 6. The typical core-shell twinned particles are obtained in the cases of Ni_{10%}/SiO₂ (1.5 equivalents of TOP) and Ni_{10%}/SiO₂^f (3 equivalents of TOP). However, for lower amount of TOP in Ni_{10%}/SiO₂^e, the morphology of the NPs is significantly different and consisting of smaller metallic Ni NPs forming filamentous morphologies by face-sharing which results in a larger coherent size of above 5 nm. It follows that, in the hot-injection synthesis, above a threshold amount of TOP, the smaller sub-particles are twinned by the encapsulating action of the TOP. However, when its amount is lower, filamentous morphologies of face-sharing metallic Ni NPs are formed similar to the Ni nanostructures obtained by dioctyl tartrate route.

Table 2. XANES Linear Combination Fit and EXAFS fit.

XANES ^[a]	Ni(0)	NiO	R-factor	Red. χ^2	
Ni- <i>hi</i>	0.38	0.62	0.0040727		
Ni- <i>dt</i>	0.614	0.386	0.0035410		
Ni _{5%} /AC	0.467	0.533	0.0033474		
Ni _{5%} /AC ^d	0.474	0.526	0.0026634		
Ni _{5%} /SiO ₂	0.634	0.366	0.0021421		
Ni _{10%} /SiO ₂	0.652	0.348	0.0023309		
Ni _{20%} /SiO ₂	0.678	0.322	0.0021674		
Ni/SiO ₂ - <i>dt</i>	0.780	0.220	0.0087291		
Ni/SiO ₂ - <i>dt-sm</i>	0.750	0.250	0.0038729		
EXAFS ^[b]	Ni(0)	NiO	R-factor	Disorder ^[c]	Red. χ^2
Ni- <i>hi</i>	0.443	0.557	0.070	0.98	332
Ni- <i>dt</i>	0.482	0.518	0.133	2.75	475
Ni _{5%} /AC	0.421	0.578	0.067	1.11	1118
Ni _{5%} /AC ^d	0.448	0.552	0.125	2.56	306
Ni _{5%} /SiO ₂	0.560	0.440	0.103	1.40	232
Ni _{10%} /SiO ₂	0.548	0.452	0.063	1.28	672
Ni _{20%} /SiO ₂	0.577	0.423	0.077	1.55	653
Ni/SiO ₂ - <i>dt</i>	0.596	0.404	0.065	1.45	657
Ni/SiO ₂ - <i>dt-sm</i>	0.607	0.393	0.133	2.75	431

[a] Linear Combination Fit performed between -20 eV and +50 eV using Ni metal and NiO as references. [b] EXAFS fit in k-range 2.5-14.5 Å⁻¹ and R-range 1-5 Å using combination of Ni-Ni scattering paths for metal up to 4th shell and one Ni-O scattering paths for oxide. [c] Value of 1 corresponds to same order than bulk oxide/metal, the higher the value the higher the disorder.

The mechanism of formation suggested above explains also the morphologies characterizing samples obtained by dioctyl tartrate route, where the stronger reducing agent leads to a faster kinetics of nucleation over growth, whereas the limited amount of capping agent (0.75 equivalents) and its hydrophobic, linear backbone

structure (as opposed to the sterically larger tetrahedral TOP) leads to a single face sharing of the smaller cluster. Figure S 3 shows X-ray diffraction (XRD) patterns of unsupported Ni-*hi* and Ni NPs supported both on silica and AC catalysts. The sharp diffraction peak at 44.3 ° and the small peak at 51.5 ° for the unsupported Ni-*hi* catalyst synthesized by hot injection method can be assigned to nickel (111) and (200) reflections of metallic Ni (PDF 65-2865). On the Ni/SiO₂-*dt* and Ni/SiO₂-*dt-sm* catalysts synthesized by dioctyl-route, broader metallic Ni diffraction peaks can be clearly observed, consistent with a smaller particle size. A reflection at 43.2 degrees 2θ can be attributed to (200) reflections in fcc NiO phases, more visible for Ni_{5%}/AC^d and Ni-*hi*, and possibly Ni_{5%}/AC.

The electronic structure analysis of the as prepared samples was performed by means of XAFS at the Ni K-edge in X-ray transmission mode, displayed in Figure 7. The XANES spectra exhibit two relevant features: [34] the resonance at ca. 8336 eV corresponding to the edge for the metallic phase; the resonance at 8352 eV corresponding to transitions of 1s to Ni4p–O2p orbitals for the oxide phase.

Reducibility of the catalysts

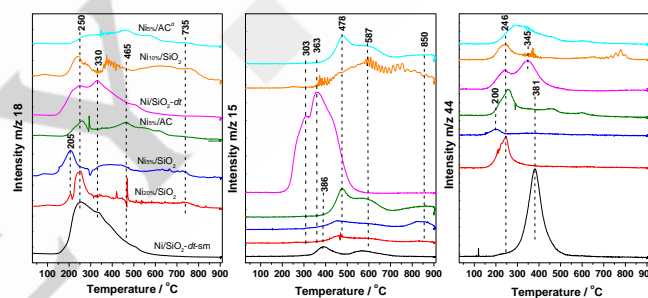


Figure 8. Evolution of *m/z* 18, 15 and 44 during TPR process, corresponding to the formation of H₂O, CH₄ and CO₂, respectively.

Accordingly, the unsupported samples are characterized by a very different electronic structure with the dioctyl route enabling NPs with more metallic character (Figure 7a). The result of the XANES linear combination fit (Table 2) shows that the unsupported NPs sample prepared by hot-injection is composed of 38% of metallic Ni and 62% of Ni²⁺, whereas the NPs sample obtained via the dioctyl tartrate route contains 61% of metallic Ni and 39% of Ni²⁺. This is indeed expected considering that the first method uses mild reducing agents whereas the second one uses a stronger reducing agent (faster nucleation step). The different nature of the ligand, more bulky and sterically hindering the TOP and, a long linear C-chain the DT, influences the particle size in the particle growth step. Differences in nuclearity among the samples are also shown by the Fourier transforms of the Ni K-edge EXAFS spectra in the inset of Figure 7a. The first peak in face-centered cubic (fcc) Ni is found at ca. 2.1 Å (non-phase corrected), whereas the peaks at higher distances in Ni-*hi* correspond to main single scattering paths of metallic Ni-Ni higher coordination shells (non-phase corrected peaks at 3.10, 3.9, 4.6 Å respectively, in Figure S4). In nickel oxide, single scattering of Ni-O and Ni-Ni are found at ca. 1.5 Å and 2.5 Å, respectively

RESEARCH ARTICLE

(insets in Figure S4). These peaks are not very pronounced for Ni-*dt* consistent with a nanostructure presenting only short-range order or comparatively lower nuclearity than the NPs in Ni-*hi*. The immobilization of the hot-injection samples on the supports leads to an increase in the percentage of metallic Ni, more so on the SiO₂ support (Figure 7b and Table 2). Whilst, only marginal differences are observed amongst the Ni_{5%}/SiO₂, Ni_{10%}/SiO₂ and Ni_{20%}/SiO₂ (Figure 7c), the seed-mediated step on the Ni/SiO₂-*dt* induces pronounced changes in terms of nuclearity consisting of a loss of long range order (Figure 7d). The structural analysis of the hot-injection samples with varying equivalents of TOP was previously reported and here included in Figure S4. It is possible to see that increasing the amount of TOP to 3 equivalents leads to small changes in the electronic structure of the samples, whereas the reduction of the TOP to 0.75 equivalents produces mostly oxide Ni nanostructures although a metallic component is seen in the FT-EXAFS spectrum.

A slight decrease in the metallic content is also observed for the seed-mediated sample. However, we should consider that differences in particle size or spatial distribution of particles could affect the fit results. To account for the structural disorder/particle size in the EXAFS fits, a disorder factor has been included in Debye Waller factors, the higher the disorder the smaller the particle size. It is possible to see that the SiO₂ support induces a higher degree of disorder, consistent with the smaller particle size. This can be explained by support effect which manifests on the smaller particles initially present as a shell of the primary particles in the NP₅ sol, which are partially dispersed on the SiO₂ support upon immobilization. Consistent with electron microscopy characterization, the disorder is significantly higher for the seed mediated sample and for the unsupported dioctyl sample.

The Ni nanoparticles supported on both activated carbon and silica catalysts were investigated using temperature programmed reduction (TPR) technique. As Ni nanoparticles after the syntheses were exposed to air, they can be easily oxidized/hydroxylated, leading to the formation of a NiOOH layer on the surface of the Ni nanoparticles, as illustrated in Figure 4. Before the TPR experiments, a pretreatment of the catalysts in argon led to water desorption, which is more pronounced for all the SiO₂-supported samples, consistent with the higher hydrophilic character of this support compared to carbon (Figure S5). Figure 8 displays the evolution of *m/z* 18, *m/z* 15 and *m/z* 44, during TPR for all the samples investigated. A more complete representation of the fragments evolved is reported in Figure S5. In the TPR process, the generation of H₂O (*m/z* 18) is thus associated with the reduction of the surface NiOOH layer on the Ni nanoparticles in the catalysts, even though it also could derive from the decomposition of organic residue at high temperatures. A three-stages reduction was reported for Ni/SiO₂: at 200–300 °C the partial reduction of large NiO particles occurs; at 300–400 °C the complete reduction of the large NiO crystallites interacting weakly with the support was reported whereas at >400 °C the complete reduction of the small NiO crystallites interacting strongly with support or the nickel silicate species was reported.^[41]

It is evident from Figure 8, that the samples obtained via hot-injection are characterized by a reduction of Ni species in a

similarly broad temperature range, spanning from easily reducible cationic Ni species around 200 °C, to relatively less reducible Ni species with a maximum up to 600 °C in the case of the carbon support. On the SiO₂ support, an additional reduction peak with maximum at 735 °C indicates the presence of highly dispersed nickel silicate species, suggesting a direct NPs/support interaction on the hot-injection samples consistent with the TEM analysis (Figure 4b). Note that some of the organic compounds employed as surfactants in the two synthesis methods of Ni nanoparticles persist in the samples after the synthesis, therefore the intensity and evolution of the signal will also be influenced by the metal exposure. For example, it is evident that Ni_{5%}/SiO₂ presents a reduction peak at the lowest temperature, which could also indicate better metal exposure effectively resulting in a higher reducibility. The profile of *m/z* 18 evolution is very different for the dioctyl tartrate route samples showing a much more abundant water evolution in the temperature range from 150 °C to 550 °C; we suggest this is due to a higher exposed surface area for these samples, consistent with the higher conversion obtained for these samples. In contrast, no species reduced at around 700 °C are present on these samples indicating a lack of direct metal/support interaction, as observed in the TEM analysis as well (Figure 5b and c).

The *m/z* 15 signal could arise from CH₃ species produced by the decomposition of organic residues on the catalysts together with the evolution of the *m/z* 44, *m/z* 28 and *m/z* 16, due to CO₂, CO and O species (from CO₂ decomposition), respectively. However, in Figure S6, *m/z* 15 evolves only at higher temperatures than the other fragments, exceeding 350 °C, over all these Ni catalysts. Therefore, *m/z* 15 can be due to methane formation from CO₂ hydrogenation over the catalyst and therefore representing the hydrogenation ability of the catalysts. The profile of this fragment depends on the preparation method as well as the support.

It is possible to note that amongst the hot-injection samples, the carbon-based ones have a similar broad and multi-peak mass evolution profile, likewise silica-based samples, whose peak maximum is shifted to a comparatively lower temperature range. For the dioctyl tartrate samples, the evolution of this fragment is shifted to even a much lower temperature range, more so for the Ni/SiO₂-*dt*.

The evolution of *m/z* 44 follows closely the *m/z* 18 profile, with peak maximum at a similar temperature and similar profile for all the catalysts but the Ni/SiO₂-*dt*-sm, which shows a single peak in the *m/z* 44 mass spectrum. More in detail, amongst the hot injection samples, the *m/z* 44 profiles indicate that the nature of the residual C overlayer is similar for all but Ni_{5%}/SiO₂ and Ni_{5%}/AC^d. The former desorbs CO₂ at lower T, the latter at higher T. For the dioctyl tartrate samples the *m/z* 44 shows a profile similar to *m/z* 15 below 500 °C (two peaks for Ni/SiO₂-*dt* and one peak for Ni/SiO₂-*dt*-sm) corroborating the postulation that *m/z* 15 is due to the hydrogenation of fragments of the decomposition of the ligands due to the methanation activity of these Ni samples.^[42-43] While there is no significant difference in the temperature peaks for H₂O formation between Ni/SiO₂-*dt* and Ni/SiO₂-*dt*-sm, the release of CO₂ (*m/z* 44) occurred at lower temperatures for Ni/SiO₂-*dt* (approximately at 246 and 345 °C) compared to Ni/SiO₂-*dt*-sm (381 °C). This indicates that the C-overlayer is of

RESEARCH ARTICLE

different nature in these two samples. We suggest that in Ni/SiO₂-dt-sm, in the second step of particles growth, the reducing agent NaBH₄, hydrogenates the O functionalities of the ligand residual from the preceding step (peak at 246 °C) which are therefore no longer observed. An intriguing observation after the TPR experiment on Ni NPs catalysts deserves a mention. The samples synthesized via the hot-injection method turned darker, indicating the occurrence of coke formation during the TPR process. Initially, H₂ reduces the NiO layer on the Ni NPs, subsequently activating the metallic Ni as centers for the decomposition of the organic residue into carbon and other species, such as CO₂, CO (N₂) and CH₃ on these catalysts. In contrast, the samples obtained via the dioctyl route exhibited a significant sintering, shanking to a small hard stone. This phenomenon may be attributed to the fact that Ni NPs were initially reduced to metallic Ni by the NaBH₄ reducing agent during synthesis, and subsequent reduction using H₂ led to severe sintering of Ni during the TPR process at high temperatures up to 900 °C. It might also be due to the oligomeric nature of the size- and morphology-controlling ligand.

Discussion

The catalytic performances presented in Figure 2 indicate a marked difference between the samples obtained via the dioctyl tartrate route and the one obtained via hot-injection, with the former one enabling to achieve much higher conversion values comparable with a commercial Ni_{18%}/Al₂O₃. The hot-injection samples suffer generally from a low conversion, except for Ni_{5%}/AC^b which was prepared using a large amount of reducing agent (OAm 15 eq.: TOP 1.5 eq.) compared to the other samples (OAm 5 eq.: TOP 1.5 eq.). On the carbon support, these systems are characterized by the primary particles covered by a shell of smaller nanoparticles embedded in an organic layer (Figure 3). The organic layer might limit the access to the active surface, leading to the low overall conversion. Additionally, 1-octadecene used as a solvent is known to polymerize under the temperature range used in these syntheses, thus lowering the amount is beneficial.^[44] However, the C-overlayer does not entirely explain the reactivity data presented herein. For example, Ni_{10%}/SiO₂^e was synthesised using 0.75 equivalents of TOP, which led to a significantly different morphology of the nanoparticles if compared with Ni_{10%}/SiO₂ synthesised using 1.5 equivalents of TOP. In a previous work,^[34] the XRD analysis over these samples was reported, which enabled us to identify more disordered oxide NPs coexisting with larger coherent metallic domains; we suggest these being the extended metallic planes in the face sharing Ni NPs agglomerates displayed in Figure 6b. However, the majority of the Ni is present as an oxide as shown in the XAFS data in Figure S3, whereas the more active and FA selective Ni_{10%}/SiO₂ presents the typical electronic features of metallic Ni NPs. The morphological characteristics in Ni_{10%}/SiO₂^e are also observed for the Ni phase in the samples obtained via the dioctyl tartrate route (Figure 5); however, Ni particles via the dioctyl tartrate route are here in a more reduced state than in the samples obtained via hot-injection. It follows that size and electronic structure play an

important role in the hydrogenation characteristics of these samples.

The reducibility of these catalysts can indeed be correlated with their performances. Higher reducibility corresponds to the higher activity of Ni_{5%}/SiO₂ (199 h⁻¹) for the hydrogenation furfural. Ni_{5%}/AC^d differs from Ni_{5%}/AC for the longer synthesis time, resulting in larger Ni particles (Figure S2). The activity for the selective hydrogenation of furfural is slightly enhanced, although it does not affect the reducibility, thereby suggesting a different Ni exposure.

Both Ni/SiO₂-dt and Ni/SiO₂-dt-sm catalysts exhibit high activity for the selective hydrogenation of furfural, as depicted in Figure 2. The higher conversion of furfural observed over the Ni/SiO₂-dt catalyst compared to Ni/SiO₂-dt-sm after 2 hours of reaction time can be attributed to the exposed active surface (Figure 5b) as well as its metallic character. This is mostly determined by the amount of the reducing agent (e.g. 15 equivalents of OAm enabled achieving high conversion with the hot-injection method, close to the dioctyl tartrate route) and its strength, with stronger reducing agents enabling smaller particle sizes thus higher exposed surface area.

Trends in selectivity amongst the samples can be explained by the synergism between the nanostructural characteristics of the exposed active metal domains and the surrounding chemical environment determined by the support as well as the C adlayers residual from the synthetic procedure. A clear example is Ni_{5%}/SiO₂. Upon immobilization of the Ni NPs from hot-injection onto the SiO₂, nanostructure changes can be observed in Figure 6 consisting of the migration of the smaller clusters of the original NPs shell onto the SiO₂ support. This is accompanied by an increase of the metallic Ni character in the sample. This correlates well with the change in performances observed from a prevalent selective hydrogenation of the unsupported particles into an unselective total hydrogenation pathway to THFI-E, for Ni_{5%}/SiO₂. Total hydrogenation was observed for larger Ni particles,^[32] consistent with the fact that the primary particles are now exposed due to the migration of the small nanoparticles. We suggest that on smaller NPs of the support, the adsorption of the reagents and the THFA product is stronger and therefore leading to the condensation reaction to form the ether; thus this system realized the optimal topological distribution of the redox Ni active phase and the acid site of the support for the synthesis of this chemical. A shift of the reduction peaks to higher T for the SiO₂-supported samples (Figures 8 and S5) coincides with a change in selectivity towards FA with increasing reaction time for Ni_{10%}/SiO₂ and Ni_{20%}/SiO₂.

In contrast, the formation of acetal is particularly pronounced at the beginning of the reaction for the activated carbon-supported samples (Ni_{5%}/AC and Ni_{5%}/AC^d) and for Ni_{10%}/SiO₂, Ni_{10%}/SiO₂^e and Ni_{20%}/SiO₂, more so for Ni_{10%}/SiO₂^e. Intuitively one could suggest that as the reaction proceed, the detachment of the C-overlayer, the reduction of the NiO and the exposure of the metal surface favors the hydrogenation pathways. However, Ni_{10%}/SiO₂^e is characterized by a lower C content, therefore it is possible to conclude that less reducible NiO species can also be responsible for the formation of the acetal as well as the subsequent condensation of the solvent with FA. Changes in selectivity must

RESEARCH ARTICLE

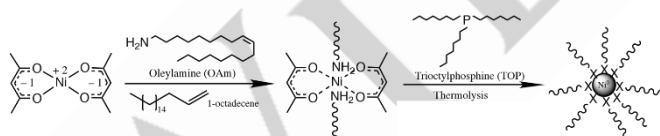
also be expected as the catalysts deactivate. In Ni_{5%}/AC^d, the increase of the selectivity towards FI-Ether at the expenses of acetal and FA formation, is consistent with a deactivation of Ni hydrogenation sites in the C matrix so that the condensation reaction of the solvent occurs now in succession to the selective hydrogenation to FA.

Conclusion

In this work, we have clarified the interplay between structural features of supported Ni NPs-based catalysts in their as synthesised state that dictates trends in time evolution of the selectivity and activity of these in the hydrogenation of furfural. Whilst metallic Ni is required for hydrogenation reaction, larger particles leads to total hydrogenation whereas smaller particles afford selective hydrogenation to FA. NiO species are instead favoring acetalization and etherification. The environment surrounding the Ni nanostructures determines also the fate of the successive reactions. Particularly, the acid sites of the support as well as the C species from either the support, a residue from the synthesis or C ad-layer formed due to coking during the reaction, will facilitate the condensation reaction of the hydroxyl alcohol functionality with the solvent. By an optimal control of these features it is possible to tune the selectivity of these systems towards the desired platform chemicals. In this work, we present a novel synthetic design which makes use of dioctyl tartrate as a shape-orienting agent for the preparation of high surface area foam-like metallic Ni-based catalyst with higher selectivity towards hydrogenation outperforming a commercial catalysts at similar conversion and activity. This is achieved in the best performing catalyst with a much lower metal loading.

Experimental Section

Synthesis of supported Ni NPs via hot-injection route using a binary ligand system consisting of oleylamine as reducing agent and trioctylphosphine as capping agent



Scheme 1. Reaction scheme for the synthesis of nickel nanoparticles via thermal decomposition reduction method from Ni(acac)₂. Image adapted from ref. [45].

List of reagents: Nickel(II) acetylacetonate (95%), oleylamine (70%), trioctylphosphine (90%) and 1-octadecene (90%) reagents were purchased from Sigma-Aldrich and used as received without further purification. CAB-O-SIL® (M-5 scintillation grade, 200 m²/g) was purchased from Acros Organics (Fisher Scientific) and used as received. Activated charcoal powder (Merck, quality 100) was used as received.

The syntheses of the samples were carried out in a round bottom flask under an atmosphere of high-purity argon to protect nickel and trioctylphosphine (TOP) from oxidation; the temperature was controlled with a thermocouple placed directly inside the reaction mixture. In a typical synthesis, a given amount of Ni(acac)₂ and oleylamine (OAm) corresponding to the targeted metal loading were mixed together in 1-octadecene (OCD) and stirred magnetically (stirring 530 rpm) at 65-70 °C in a flow of Ar under reflux conditions. Once the mixture was completely dissolved, TOP degassed with N₂ for 10 minutes, was rapidly injected into the flask, followed by re-setting the temperature to 120 °C and holding it for 10 minutes. The mixture was then rapidly heated to 220 °C over the course of 15 minutes for nucleation and ripening of the nanoparticles. If not otherwise indicated, the synthesis was halted after 2 hours of reflux under stirring (530 rpm), and the flask cooled to room temperature. For the supported NPs samples, the suspension containing the nickel nanoparticles was then added to a suspension of either silica (CAB-OSIL 5 M) or activated charcoal in absolute ethanol (150 mL), under vigorous stirring. The mixture was then filtered under vacuum and washed multiple times with copious amount of ethanol until the filtrate was colourless, indicating removal of excess surfactants. Amounts of Ni(acac)₂ precursor, OAm, TOP, 1-octadecene and SiO₂ support were adjusted to obtain ca. 4 g of sample with a nominal NPs loading of 5%, 10 wt% and 20% (expressed in metal weight).

Synthesis of supported Ni NPs using dioctyl tartrate as capping agent and sodium borohydride as reducing agent

List of reagents: (R,R)-tartaric acid (ACS reagent, ≥99.5%), 1-octanol (ReagentPlus®, 99%), ethyl acetate (HPLC Plus, 99.9%), –hexane (anhydrous, 95%), concentrated HCl (ACS reagent, 37%), NiBr₂ (anhydrous 98%), absolute ethanol (≥99.8%), sodium borohydride (powder, ≥98.0%) were purchased from Sigma Aldrich and used as received.

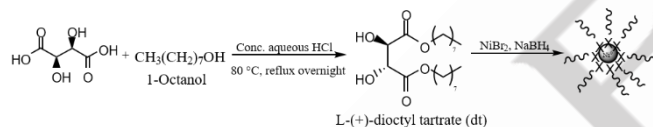
Firstly, the dioctyl tartrate capping agent was synthesised following a procedure reported in the literature.^[46] Accordingly, a solution of (R,R)-tartaric acid (7.69 g, 51.24 mmol) and concentrated HCl (1.5 mL) in 1-octanol (100 mL) was heated at 80 °C in reflux overnight. Then, the octanol in excess was then distilled off under vacuum and purified by column chromatography (eluent: ethyl acetate–hexane 1 : 3 v/v) to afford the title compound (16.57 g, 86%) as a white solid. δ_H (400.1 MHz; CDCl₃; Me₄Si) 4.55 (d, ³J_{HH} 6.4 Hz, 2H, CHOH), 4.28 (td, ³J_{HH} 6.74, 2.72 Hz, 4H, OCH₂CH₂), 3.17 (d, ³J_{HH} 7.1 Hz, 2H, CHOH), 1.71 (p, ³J_{HH} 6.6 Hz, 4H, OCH₂CH₂), 1.43 – 1.28 (m, 20H, OCH₂CH₂(CH₂)₆), 0.90 (t, ³J_{HH} 8.0 Hz, 6H, CH₃). δ_C (100.6 MHz; CDCl₃; Me₄Si) 171.6 (C=O, C-9), 72.0 (CHOH, C-10), 66.6 (OCH₂, C-8), 31.8 (C-3), 29.1 (C-4, C-5), 28.5 (C-7), 25.7 (C-6), 22.6 (C-2), 14.1 (CH₃, C-1).

RESEARCH ARTICLE

To prepare nickel nanoparticles supported on silica (20 wt%) with L-(+)-dioctyl tartrate as capping agent, NiBr₂ (2.98 g, 13.63 mmol) and L-(+)-dioctyl tartrate (3.83 g, 10.22 mmol) were dissolved under vigorous stirring in ethanol (100 mL). Sodium borohydride (2.59 g, 68.46 mmol) dissolved in 100 mL of ethanol was then added dropwise to this solution at room temperature over the course of 15 minutes under stirring (650 rpm), resulting in the immediate reduction of Ni²⁺ as observed by a colour change of the yellow-brown solution to black. To prepare the supported NP_s samples, the nanoparticles suspension was added to a suspension of 3.2 g of SiO₂ in 150 mL ethanol as described above.

A “seed-mediated”/sequential synthesis was carried out as follows. 0.60 g of NiBr₂ and 0.77 g of L-(+)-dioctyl tartrate were dissolved in 20 mL of ethanol. Then, 0.52 g of NaBH₄ were dissolved in 20 mL of ethanol. A seed solution was prepared by mixing these two solutions under stirring for 4 h to ensure complete decomposition of the reducing agent. A growth solution was prepared in the same way but using 2.83 g of NiBr₂ and 3.63 g of L-(+)-dioctyl tartrate in 100 mL of ethanol, to which a solution of NaBH₄ (2.44 g) in 100 mL of ethanol was slowly added dropwise at room temperature.

Subsequently, 10 mL of the seed solution were added to the growth solution and left under stirring for 4h. The NPs suspension was added to CAB-O-SIL 5M (3.2 g) as described above.



Scheme 2. Reaction scheme for the synthesis of nickel nanoparticles via diocetyl tartrate route.

Catalyst characterization

The ICP-OES technique (Spectrogreen FMD46) was used to determine Ni loadings of the catalysts. Before analysis, solid catalysts were dissolved in acid using a Digiprep JR (SCP-SCIENCE) digester. XRD patterns of the catalysts were obtained using a Bruker diffractometer (model D8 Advance-A25) with a Cu-K α_1 radiation source (wavelength of 1.54 Å) operating at 40 kV and 40 mA. Scans were collected over the range of 10° to 90°.

X-ray absorption fine structure spectra at the Ni K-edge were obtained at the B18 beamline at Diamond Light Source, UK.^[47] The measurements were carried out using a fixed-exit double-crystal Si(111) monochromator and the Pt-coated branch of collimating and focusing mirrors. Harmonic rejection mirrors were placed in the beam path and used as a low-pass filter to remove

higher energy harmonics. The beam size at the sample position was approximately 1x1 mm. All samples were prepared in form of pellets (13 mm diameter) mixing 50 mg of sample with 50 mg of cellulose to optimize the edge jump and total transmission. The measurement was performed at room temperature in transmission mode using 3 ion chambers filled with following gases: 300 mbar N₂ + 700 mbar He (I0); 150 mbar Ar + 850 mbar He (I1, I2). The spectra were collected in quick EXAFS mode by continuously scanning the monochromator with a constant energy step size of 0.3 eV. The scan covered an energy range from 8133.15 to 9333 eV, corresponding to a k-range of 16Å⁻¹. For each sample, 3 scans were acquired and subsequently merged to improve the signal to noise ratio. Data were normalised using the program Athena^[48] with a linear pre-edge and 2nd order polynomial post-edge. After background subtraction, the resulting $\chi(k)$ functions were k²-weighted and Fourier transformed in a range from 2 to 15.5 Å⁻¹. The EXAFS fit was performed using the two references structures, Ni0 and NiO, for which the most relevant single and multiple scattering paths were calculated. The amplitude of each signal was then described as a function of the ratio of the phases generating the scattering path and the ratios optimized during the fit of the experimental data.

Bright field (BF) and high angle annular dark field scanning transmission electron microscopy (HAADF-STEM) images were acquired on a probe and image corrected Titan Themis³ operated at an acceleration voltage of 200 keV. The HAADF-STEM imaging technique is highly sensitive to the atomic number of elements, and the intensity observed in the images is proportional to the square of the atomic number (Z²). This enables the differentiation of small nanoparticles and even single atoms supported on light materials, making it an invaluable tool for high-resolution imaging. Elemental mapping using energy dispersive X-ray spectroscopy (EDX) to determine the distribution of elements was also performed. Those experiments were conducted using a beam current of 200 pA and a dwell time per pixel of 128 μ s. Finally, we applied a Gaussian blur of 0.8 using Velox software to improve the visual quality of the elemental maps. The Ni samples were deposited onto 3 mm holey carbon Cu-grids for TEM analysis.

Temperature Programmed Reduction (TPR) experiments were conducted in a U-shaped quartz reactor filled with approximately 90 mg of catalysts. The samples were heated to 150 °C at a rate of 10 °C/min and held at this temperature for 1 hour in a flow of Ar (60 mL/min) to eliminate adsorbed H₂O in the catalysts. After the reactor cooled down to room temperature, a flow of 5% H₂/Ar at 60 mL/min was introduced and the reactor heated to 900 °C at a rate of 10 °C/min and maintained at 900 °C for 0.5 hours. The outlet of the reactor was connected to a mass spectrometer (Pfeiffer Vacuum, Prisma Plus) to monitor product evolution. To this goal, the temperature and *m/z* signals of 2, 15, 18, 28 and 44 were recorded.

RESEARCH ARTICLE

Hydrogenation reaction

The liquid phase hydrogenation of furfural was performed using a stainless-steel autoclave equipped with a heater and a magnetic stirrer at 6 bar and 180 °C. The required amount of catalyst (Ni/furfural=1/500 mol/mol) along with a furfural solution (10 mL, 0.3 M in isopropanol as the solvent) was loaded into the reactor for a typical experiment. The sealed reaction vessel was purged three times with N₂, and three times with H₂ before being pressurized to 6 bar with H₂. Once the temperature reached to 180 °C, the autoclave was then stirred at 1200 rpm. At regular intervals, the reaction was stopped by turning down the stirring and reaction samples (0.2 mL) were taken and mixed with the internal solvent (2-propanol) and the external standard (dodecanol) for analysis. The reaction was stopped after 4 h, and the reaction mixture was cooled to room temperature and centrifuged prior to being analyzed by gas chromatography (Agilent 6890, equipped with a Zebron ZB5 60 m x 0.32 mm x 1 μm column and a FID detector, Agilent, Santa Clara, CA, USA). Response factors of the furfural and obtained products were calculated using a known concentration of the pure compound's standard solutions. Gas chromatography–mass spectrometry (GC-MS) was used to identify unknown products (Thermo Scientific ISQ QD, fitted with an Agilent VF-5ms column; 60 m x 0.32 mm I.D x 1 mm, Thermo Scientific, Waltham, MA, USA).

We calculated the conversion using equation (1):

$$\text{Conversion (\%)} = \frac{mol_i - mol_t}{mol_i} \cdot 100 \quad (1)$$

Where mol_i are the initial moles of furfural and mol_t are the moles after a reaction time “t”. The selectivity was calculated using equation (2):

$$\text{Selectivity}_i (\%) = \frac{mol_i}{\sum mol_t} \cdot 100 \quad (2)$$

Where mol_i are the moles of product “i” and $\sum mol_t$ is the sum of the moles of all the other reaction products.

The initial catalytic activity was calculated using equation (3) on the total amount of active metal:

$$\text{Activity (h}^{-1}\text{)} = \frac{mol_i - mol_{15}}{mol_{Ni}} \cdot \frac{60}{t} \quad (3)$$

Where mol_{15} are the moles after 15 minutes of reaction, mol_{Ni} are the moles of Ni loaded in the reactor and t is the reaction

time (15 minutes). The AC and SiO₂ supports were also tested and gave 0% and 3% conversion, respectively,

Acknowledgements

SG acknowledges the Year in Industry placement scheme at Diamond Light Source (2017–18, “Chirally modified catalyst nanoparticles” project on the VERSOX beamline in collaboration with the UK Catalysis Hub) and the External Placement scheme of the School of Chemistry in the University of St Andrews. We thank DLS for the allocation of beamtime under the proposal SP28630. The UK Catalysis Hub is thanked for resources and support provided via our membership of the UK Catalysis Hub Consortium and funded by EPSRC grants: EP/R026939/1, EP/R026815/1, EP/R026645/1, EP/R027129/1 or EP/M013219/1. XC and JJD would like to thank the financial support by MINECO (Spain) through project PID2020-113809RB-C33.

Keywords: Ni nanoparticles • Furfural hydrogenation • Ni K edge XANES • HAADF-STEM

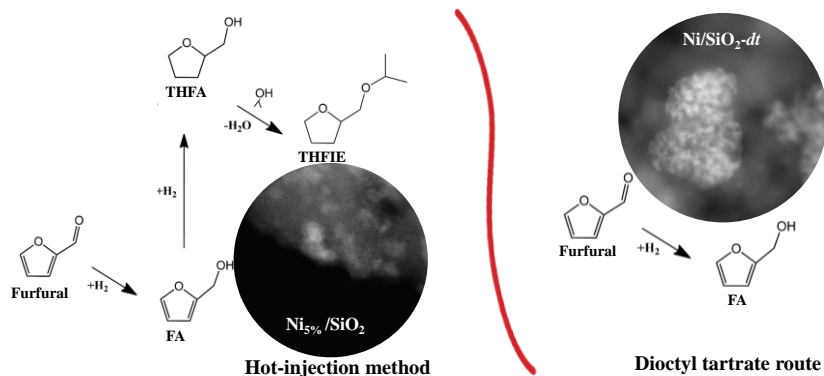
- [1] J. McGlone, P. Priece, L. Da Vià, L. Majdal, J.A. Lopez-Sanchez, *Catalysts*. **2018**, 8.
- [2] P. Gallezot, *Chem. Soc. Rev.* **2012**, 41, 1538–1558.
- [3] H. Paysepar, K.T.V. Rao, Z. Yuan, L. Nazari, H. Shui, C. (Charles) Xu, *Fuel Process. Technol.* **2018**, 178, 362–370.
- [4] R. Mariscal, P. Maireles-Torres, M. Ojeda, I. Sádaba, M. López Granados, *Energy Environ. Sci.* **2016**, 9.
- [5] S. Alijani, S. Capelli, S. Cattaneo, M. Schiavoni, C. Evangelisti, K.M.H. Mohammed, P.P. Wells, F. Tessore, A. Villa, *Catalysts*, **2020**, 10, 1–16.
- [6] M.J. Taylor, L.J. Durndell, M.A. Isaacs, C.M.A. Parlett, K. Wilson, A.F. Lee, G. Kyriakou, *Appl. Catal. B Environ.* **2016**, 180, 580–585.
- [7] B.M. Barbosa, J.L. Colodette, D. Longue Júnior, F.J.B. Gomes, D.C. Martino, *J. Wood Chem. Technol.* **2014**, 34, 178–190.
- [8] G. Machado, S. Leon, F. Santos, R. Lourega, J. Dullius, M.E. Mollmann, P. Eichler, *Nat. Resour.* **2016**, 07, 115–129.
- [9] a) Chem. Eng. J. 436 (2022) 135070, 32–40; b) ChemCatChem2022,14, e2021017
- [10] a) S. Sitthisa, T. Pham, T. Prasomsri, T. Sooknoi, R. G. Mallinson, D. E. Resasco, *Journal of Catalysis* **2011**, 280, 17-27; b) K. Yan, G. Wu, T. Lafleur, C. Jarvis, *Renewable and Sustainable Energy Reviews* **2014**, 38, 663-676.
- [11] X. Li, P. Jia, T. Wang, *ACS Catal.* **2016**, 6 (11), 7621–7640.
- [12] Z. An, J. Li, *Green Chem.*, **2022**, 24, 1780-1808.
- [13] P. Guo, S. Liao, X. Tong, *ACS Omega* **2019**, 4, 21724–21731.
- [14] T. V. Kotbagi, H.R. Gurav, A.S. Nagpure, S. V. Chilukuri, M.G. Bakker, *RSC Adv.* **2016**, 6, 67662–67668.
- [15] K. Yang, R. Wang, D. Xu, X. Ma, D. Ding, M. Zhang, L. Zhang, Z. Bai, Z. Zhu, H. Lü, *Journal of catalysis* **2023**, 425, 170-180.
- [16] D. Wu, W. Y. Hernández, S. Zhang, E. I. Vovk, X. Zhou, Y. Yang, A.Y. Khodakov, V. V. Ordonsky, *ACS Catal* **2019**, 9, 2940-2948.
- [17] O'Driscoll, J.J. Leahy, T. Curtin, *Catal. Today*. **2017**, 279, 194–201.
- [18] C. Wang, Z. Guo, Y. Yang, J. Chang, A. Borgna, *Eng. Chem. Res.* **2014**, 53, 11284–11291.
- [19] S. Bhogeswararao, D. Srinivas, *J. Catal.* **2015**, 327, 65–77.

RESEARCH ARTICLE

- [20] S.T. Thompson, H.H. Lamb, *ACS Catal.* **2016**, 6, 7438–7447.
- [21] T.P. Sulmonetti, S.H. Pang, M.T. Claire, S. Lee, D.A. Cullen, P.K. Agrawal, C.W. Jones, *Appl. Catal. A Gen.* **2016**, 517, 187–195.
- [22] F. Liu, Q. Liu, J. Xu, L. Li, Y.T. Cui, R. Lang, L. Li, Y. Su, S. Miao, H. Sun, B. Qiao, A. Wang, F. Jérôme, T. Zhang, *Green Chem.* **2018**, 20.
- [23] F. Atsushi, P.L. Dhepe, *Chem. Rec.* **2009**, 9, 224–235.
- [24] S.M. Rogers, C.R.A. Catlow, D. Gianolio, P.P. Wells, N. Dimitratos, *Faraday Discuss.* **2018**, 208, 443–454.
- [25] A. Guerrero-Torres, C.P. Jiménez-Gómez, J.A. Cecilia, C. García-Sancho, F. Franco, J.J. Quirante-Sánchez, P. Maireles-Torres, *Top. Catal.* **2019**, 62, 535–550.
- [26] H. Jeong, C. Kim, S. Yang, H. Lee, *J. Catal.* **2016**, 344, 609–615.
- [27] L. Liu, H. Lou, M. Chen, *Int. J. Hydrogen Energy.* **2016**, 41, 14721–14731.
- [28] W. Gong, C. Chen, H. Wang, R. Fan, H. Zhang, G. Wang, H. Zhao, *Chinese Chem. Lett.* **2018**, 29, 1617–1620.
- [29] S. Carencio, C. Boissière, L. Nicole, C. Sanchez, P. Le Floch, N. Mézailles, *Chem. Mater.* **2010**, 22, 1340–1349.
- [30] R. Rinaldi, A. de Melo Porcari, T. C.R. Rocha, W. H. Cassinelli, R. Uema Ribeiro, J. Maria Correa Bueno, D. Zanchet, *Journal of Molecular Catalysis A: Chemical*, **2009**, 301, 11–17.
- [31] Y. Nakagawa; H. Nakazawa; H. Watanabe; K. Tomishige, *ChemCatChem* **2012**, 4, 1791–1797.
- [32] X. Meng; Y. Yang; L. Chen; M. Xu; X. Zhang; M. Wei, *ACS Catal.* **2019**, 9, 4226–4235.
- [33] E. Zacharaki, P. Beato, R.R. Tiruvalam, K.J. Andersson, H. Fjellvåg, A.O. Sjøstad, *Langmuir* **2017**, 33, 9836–9843.
- [34] R. Arrigo, S. Gallarati, M. E. Schuster, J. M. Seymour, D. Gianolio, I. da Silva, J. Callison, H. Feng, J. E. Proctor, P. Ferrer, F. Venturini, D. Grinter, G. Held, *ChemCatChem*, **2020**, 12, 1491–1503.
- [35] L. Zhu, S. Ye, J.g Zhu, C. Duan, K. Li, G. He, X. Liu, *ACS Sustainable Chem. Eng.* **2022**, 10, 32, 10526–10536.
- [36] L.-P. He, S.-Y. Sun, Y.-Y. Mu, X.-F. Song, J.-G. Yu, *ACS Sustainable Chem. Eng.* **2017**, 5, 1, 714–721.
- [37] J. Xu, Q. Cui, T. Xue, Y. Guan, P. Wu, *ACS Omega* **2020**, 5, 46, 30257–30266.
- [38] Y. Wang, D. Zhao, D. Rodríguez-Padrón, C. Len, *Catalysts* **2019**, 9, 796.
- [39] P. Balla, P. K. Seelam, R. Balaga, R. Rajesh, V. Perupogu, T. X. Liang, *Journal of Environmental Chemical Engineering* **2021**, 9, 106530.
- [40] R. Arrigo, S. Wrabetz, M. E. Schuster, D. Wang, A. Villa, D. Rosenthal, F. Girsgdies, G. Weinberg, L. Prati, R. Schlögl, D. S. Su, *Phys. Chem. Chem. Phys.*, **2012**, 14, 10523–10532.
- [41] F. Yang, D. Liu, Y. Zhao, H. Wang, J. Han, Q. Ge, X. Zhu, *ACS Catal.* **2018**, 8, 1672–1682.
- [42] C. Mebrahtu, F. Krebs, G. Giorgianni, S. Abate, S. Perathoner, G. Centi, A. I. Large, G. Held, R. Arrigo, R. Palkovits, *Chem. Eng. Res. Design*, **2023**, 193, 320–339
- [43] G. Giorgianni, C. Mebrahtu, M. Erwin Schuster, A. Ian Large, G. Held, P. Ferrer, F. Venturini, D. Grinter, R. Palkovits, S. Perathoner, G. Centi, S. Abate, R. Arrigo, *Physical Chemistry Chemical Physics*, **2020**, 34, 18788–18797.
- [44] E. Dhaene, J. Billet, E. Bennett, I. Van Driessche, J. De Roo, *Nano Lett.* **2019**, 19, 10, 7411–7411.
- [45] J. Park, E. Kang, S. U. Son, H. M. Park, M. K. Lee, J. Kim, K. W. Kim, H. J. Noh, J. H. Park, C. J. Bae, J. G. Park and T. Hyeon, *Adv. Mater.*, **2005**, 17, 429–434.
- [46] J. L. M. van Nunen, B. F. B. Folmer and R. J. M. Nolte, *J. Am. Chem. Soc.*, **1997**, 119, 283–291.
- [47] A. Dent, G. Cibin, S. Ramos, A. Smith, S. Scott, L. Varandas, M. Pearson, N. Krumpa, C. Jones, P. Robbins, *J. Phys. Conf. Ser.* **2009**, 190, 012039.
- [48] B. Ravel, M. Newville, *J. Synchrotron Radiat.* **2005**, 12, 537–541

RESEARCH ARTICLE

Entry for the Table of Contents



Two methods have been developed to synthesize Ni nanoparticles with unique morphological and electronic properties. They have been supported on activated charcoal and fumed silica, each displaying distinct metal-support interactions. The hot-injection method yields catalysts suitable for the full hydrogenation of furfural, while those synthesized via the diocetyl tartrate route exhibit excellent selectivity for the selective hydrogenation of the aldehyde group of furfural.

Institute and/or researcher Twitter usernames: ((optional))